Electron contamination modeling and reduction in a 1 T open bore inline MRI-linac system

B. M. Oborn
Illawarra Cancer Care Centre (ICCC), Wollongong, NSW 2500, Australia and Centre for Medical Radiation Physics (CMRP), University of Wollongong, Wollongong, NSW 2500, Australia

S. Kolling
Sydney Medical School, University of Sydney, NSW 2006, Australia

P. E. Metcalfe
Centre for Medical Radiation Physics (CMRP), University of Wollongong, Wollongong, NSW 2500, Australia and Ingham Institute for Applied Medical Research, Liverpool, NSW 2170, Australia

S. Crozier
School of Information Technology and Electric Engineering, University of Queensland, QLD 4072, Australia

D. W. Litzenberg
Department of Radiation Oncology, University of Michigan Hospital and Health Systems, Ann Arbor, Michigan 48109

P. J. Keall
Sydney Medical School, University of Sydney, NSW 2006, Australia and Ingham Institute for Applied Medical Research, Liverpool, NSW 2170, Australia

(Received 28 October 2013; revised 18 February 2014; accepted for publication 31 March 2014; published 21 April 2014)

Purpose: A potential side effect of inline MRI-linac systems is electron contamination focusing causing a high skin dose. In this work, the authors reexamine this prediction for an open bore 1 T MRI system being constructed for the Australian MRI-Linac Program. The efficiency of an electron contamination deflector (ECD) in purging electron contamination from the linac head is modeled, as well as the impact of a helium gas region between the deflector and phantom surface for lowering the amount of air-generated contamination.

Methods: Magnetic modeling of the 1 T MRI was used to generate 3D magnetic field maps both with and without the presence of an ECD located immediately below the MLC's. Forty-seven different ECD designs were modeled and for each the magnetic field map was imported into Geant4 Monte Carlo simulations including the linac head, ECD, and a $30 \times 30 \times 30$ cm^3 water phantom located at isocenter. For the first generation system, the x-ray source to isocenter distance (SID) will be 160 cm, resulting in an 81.2 cm long air gap from the base of the ECD to the phantom surface. The first 71.2 cm was modeled as air or helium gas, with the latter encased between two windows of 50 μm thick high density polyethlyene. 2D skin doses (at 70 μm depth) were calculated across the phantom surface at 1×1 mm^2 resolution for 6 MV beams of field size of 5×5, 10×10, and 20×20 cm^2.

Results: The skin dose was predicted to be of similar magnitude as the generic systems modeled in previous work, 230% to 1400% of D_{max} for 5×5 to 20×20 cm^2, respectively. Inclusion of the ECD introduced a nonuniformity to the MRI imaging field that ranged from ~20 to ~140 ppm while the net force acting on the ECD ranged from ~151 N to ~1773 N. Various ECD designs were 100% efficient at purging the electron contamination into the ECD magnet banks; however, a small percentage were scattered back into the beam and continued to the phantom surface. Replacing a large portion of the extended air-column between the ECD and phantom surface with helium gas is a key element as it significantly minimized the air-generated contamination. When using an optimal ECD and helium gas region, the 70 μm skin dose is predicted to increase moderately inside a small hot spot over that of the case with no magnetic field present for the jaw defined square beams examined here. These increases include from 12% to 40% of D_{max} for 5×5 cm^2, 18% to 55% of D_{max} for 10×10 cm^2, and from 23% to 65% of D_{max} for 20×20 cm^2.

Conclusions: Coupling an efficient ECD and helium gas region below the MLCs in the 160 cm isocenter MRI-linac system is predicted to ameliorate the impact electron contamination focusing has on skin dose increases. An ECD is practical as its impact on the MRI imaging distortion is correctable, and the mechanical forces acting on it manageable from an engineering point of view.
 [http://dx.doi.org/10.1118/1.4871618]

Key words: MRI-linac, electron contamination, skin dose, Monte Carlo simulation, magnetic deflector

1. INTRODUCTION

Magnetic resonance imaging (MRI)-guided radiotherapy as delivered by an MRI-linac (MRL), is showing promise as potentially a major advance in cancer radiotherapy. First, the modality will offer real time MR-quality images of the patient anatomy. Second, when coupled with the dynamic real time operation of a multleaf collimator (MLC) modulated radiotherapy beam, there is the expectation that moving tumors can be treated with the tightest margins. The end result would be a reduction in dose to healthy tissue - lower toxicity, while at the same time dose escalation to the tumor - higher local control rates. In essence this is a more ideal radiotherapy treatment.

At present the group from UMC Utrecht have a second generation MRI-linac system consisting of a Philips 1.5 T closed bore MRI and an Elekta 6 MV linac.[1] At the Cross Cancer Institute, a bidirectional linac-MR system consisting of a Varian linac (6 MV) and a 0.56 T MRI system[2] is being built. Although technically not an MRI-linac, the ViewRay[3] system is a related device comprised of three Cobalt-60 radiation sources within a 0.35 T MRI scanner. Finally, as elaborated in this work, a 1 T open bore MRI-linac system is under development at the Ingham Research Institute, Sydney Australia. This system will utilize a Varian based 6 MV x-ray beam and 120 leaf MLC, and a custom designed 1 T open bore MRI system built by Agilent Technologies, Oxford, United Kindom.

This particular open bore design was first envisaged in the related 2011 work by Constantin *et al.*[4] In that work, a 0.5 T GE Signa split bore MRI system was modeled for its impact on electron guns operating inside the fringe field of the MRI.

The Sydney system is similarly designed to operate without any magnetic shielding of the linac head. The MRI field has been specially designed to include low magnetic field regions (~ 0 T) where the linac x-ray target and waveguide will lie. Further to this, the generation I system will not rotate the linac—instead a rotating couch is planned.

For the purposes of this work, we will define an open bore MRI system as one which has the magnetic field source coils separated into two halves such that a patient could be placed through or between the gap. Thus a patient could be exposed to a radiation beam that travels down the bore and is parallel or inline with the MR imaging field at the isocenter: inline MRIgRT. This type of system however still inherently allows a patient to be placed inside the bore and a radiation beam travel through the gap perpendicular to the magnetic field direction: perpendicular MRIgRT. Both the Alberta and the Sydney designs are therefore open bore designs, and are both planned for testing in the inline and perpendicular orientations.

Some drawbacks for MRI-guided radiotherapy include first the complexity of the engineering feat required to make an MRI-linac system operate as intended, and second accounting for the x-ray dose deposition changes induced by the magnetic field of the MRI scanner. A third drawback that is arguably not fully realized at this point in time is that of the quality assurance or dose delivery confirmation of such a system.

In terms of skin dose changes several studies have focused on this in both the perpendicular and inline orientations.[5–9] Of particular interest are the recent simulations performed by our group which predicted that the fringe field from an inline 1 T MRI-linac system could act to focus electron contamination from the linac head, resulting in large skin dose increases at the patient/phantom surface.[7] The focusing of electron contamination from a linac generated x-ray beam in a parallel magnetic field has been most notably first experimentally reported more than a decade ago,[10] and later confirmed to match with simulations of the same arrangement.[11] In that work, a 20 cm bore superconducting solenoid magnet was used to generate a strong magnetic field parallel to a 10 MV photon beam with a distance from the x-ray source to magnet center of 250 cm. Film measurements showed a large but not quantitatively evaluated increase in the beam entry side surface dose. These film data have now been reprocessed in this current work to ascertain the magnitude, see Sec. 3.A.

A technique used to lower the production of air-generated contamination in the extended air-column of the Litzenberg experiment was replacement of the air with helium gas. This is a well known method being described as early as 1979.[12] This has been experimentally proven in various works since 1979.[13–18] Removal or purging of electron contamination from radiotherapy x-ray beams via some type of permanent or electromagnet system has also a long and mostly successful history.[14,15,17–28]

The aim of this work is to reinvestigate our previous modeling predictions of high skin dose by accurately modeling the 1 T open bore MRI design which is now under construction. We also report on the use of a permanent magnet electron contamination deflector (ECD) system, located below the MLCs, to purge electron contamination arising from the linac head and collimation system. Finally, we aim to investigate the impact of replacing a large portion of the air column between the ECD and phantom surface with helium gas as a method of minimizing the amount of air-generated electron contamination that will otherwise transport directly to the phantom surface due to the strong parallel magnetic field of the MRI.

In this current simulation work, we have additional constraints on the properties of the electron contamination deflector. These constraints include the ability to generate a transverse magnetic field strong enough to deflect contamination while being subject to the background MRI fringe field, and second minimize the impact on the MR imaging uniformity. In order to have confidence in answering these questions, full Monte Carlo simulations of the linac head are performed which utilize accurate magnetic field maps taken from finite element modeling of the actual MRI and electron contamination deflector designs.

2. MATERIALS AND METHODS

2.A. Benchmark magnetic modeling of the MRI design

COMSOL Multiphysics[29] was used to set up a finite element model of the 1 T open bore MRI system which is currently under construction. The coil currents and

configurations were modeled as provided by the manufacturer Agilent. In the first benchmarking simulations, no ferromagnetic objects were included and the goal was to match the Agilent specifications, namely, the properties of the imaging field and fringe field. In the imaging field, or the diameter of spherical volume (DSV) the most important quantity is the uniformity of the magnetic field in the z-direction, B_z. This uniformity is ±0.5 ppm (20 cm DSV) and ±5 ppm (30 cm DSV). A key design feature of the fringe field is low strength regions in both the inline and perpendicular systems where the linac will reside.

The boundary condition $\vec{n} \cdot \vec{B} = 0$ was set at the boundary of the largest cylinder to encompass a finite size to the simulated volume. In the final model there were 14×10^6 mesh elements, with around 90% of these inside an air volume of 6 m × 6 m (length×diameter) symmetric cylinder surrounding the coils.

Mesh size independence of the model was confirmed by a converging result with increasing resolution of the mesh size. This process is described in detail in recent work by our group.[30]

The solver used was the stationary solver FGMRES, and the coils were described as External Current Density sources under the magnetic fields interface indentifier which is part of the AC/DC physics module of COMSOL. In this benchmarking work, a full 3D model was employed, similar to the non-symmetric models which included the ECD (see Sec. 2.B). When solved the simulation took around 240 CPUh on 2.6 GHz AMD processors. The RAM required was around 200 GB.

2.B. Electron contamination deflector (ECD) magnetic modeling

A permanent magnet style electron contamination deflector system located below the MLC's was next included in the COMSOL simulations. This consisted of 2 banks of NdFeB (grade N38) rare-earth magnets with a plain carbon steel grade 1010 magnetic circuit to encourage flux to cross the magnet gap (see Fig. 1). The B-H curve of this material was sourced from the material library of the Ansys Maxwell3D software (Canonsburg, PA). The device was modeled with a fixed gap to allow a maximum field size of 20 × 20 cm^2 to pass through without interference. The magnet bank thickness, steel thickness, and magnet depth were varied. The values investigated were magnet bank thickness: 1 cm, 2 cm, 3 cm, 4 cm, and 5 cm; steel thickness: 0.5 cm, 1 cm, 1.5 cm, 2.0 cm, and 2.5 cm; ECD depth: 4 cm, 6 cm, and 8 cm. This resulted in the least massive design having 0.64 kg of NdFeB and 0.736 kg of steel 1010, and the most massive model having 6.4 kg of NdFeB and 5.44 kg of steel 1010. The impact of the ECD on the 30 cm diameter DSV uniformity was calculated for each combination.

Inside COMSOL, the ECD steel was modeled as a case of Amperes' Law using the steel grade 1010 magnetization (BH) curve under the magnetic fields interface indentifier (AC/DC

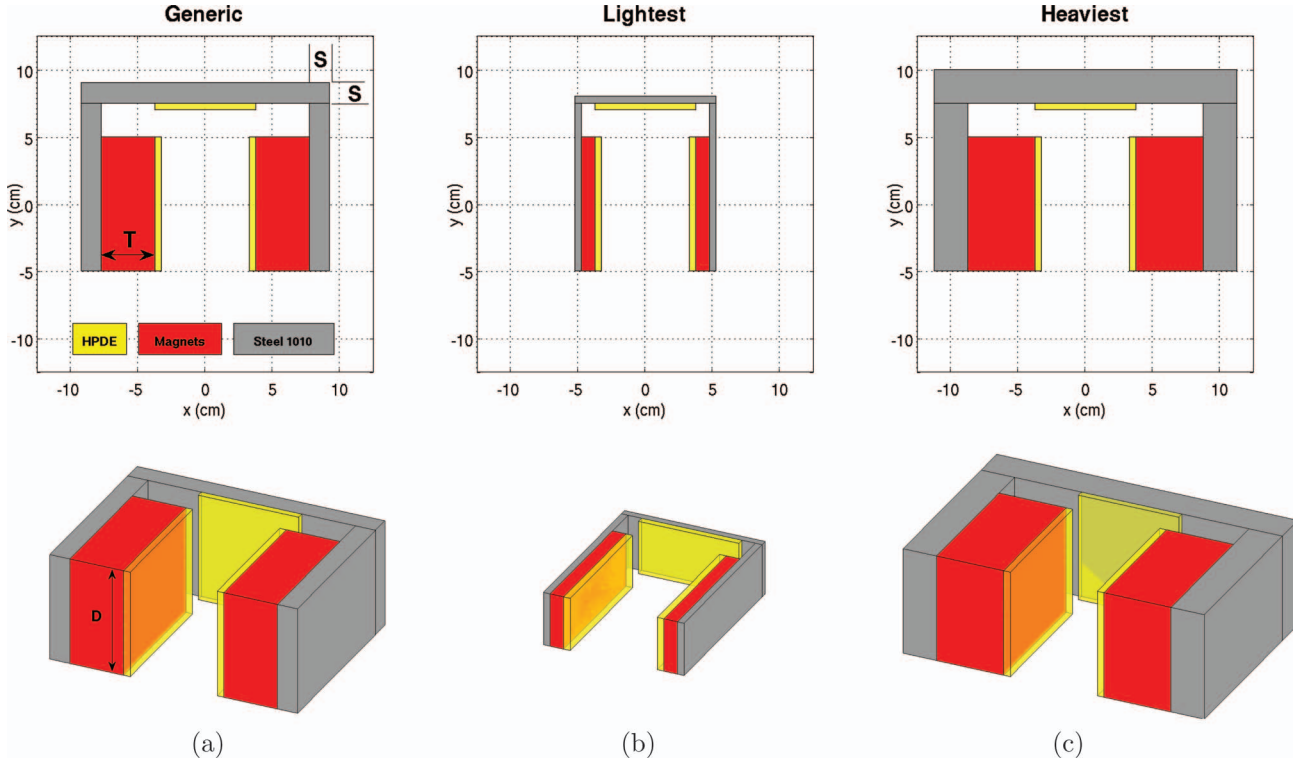

FIG. 1. Schematic diagram of the electron contamination deflector (ECD). (a) Generic design showing the dimensions which were modeled heuristically: magnet thickness (T), steel thickness (S), magnet and steel depth (D). (b) The least massive ECD modeled: 0.64 kg of NdFeB and 0.736 kg of steel 1010. (c) The most massive ECD modeled: 6.4 kg of NdFeB and 5.44 kg of steel 1010. Each design has a 5 mm thick high density polyethlyene (HDPE) cover on the magnet surfaces facing the CAX as well as a portion of the steel circuit. The HDPE cover is designed to minimize deflected electrons scattering back in the x-ray beam.

physics module) while the permanent magnets were also set up as a case of Amperes' Law with a remanent flux density of 1.3 T and relative permeability of 1.05 as per the specifications of N38 grade NdFeB permanent magnets. For each simulation a Force Calculation node was included to calculate the net force acting on the ECD as a whole unit.

Meshing of this model included dedicated air volumes surrounding just the ECD. This improved mesh generation and minimized RAM requirements as much as possible while preserving the desired accuracy. When solved the simulations including the ECD designs took around 720 CPUh on 2.6 GHz AMD processors. The RAM required was around 220 GB.

2.C. Monte Carlo simulations

The Monte Carlo simulations were performed using Geant4.9.6.p02.[31] The physics processes used were the Livermore models and for electron stepping inside a magnetic field the 4th-order Runge-Kutter stepper was used. This stepping algothrim has been successfully benchmarked in the work by Raaijmakers *et al.*[32] The beam modeled was a 6 MV (Varian 2100C) photon beam.[33] The accuracy of this linac head model has been confirmed in previous work[5] for the Geant version 4.9.1. The same benchmarking measurements were repeated with version 4.9.6p02 and results were essentially identical. For all simulations, a phase space file was used as the input particles. The phase space was located at a plane at the base of the flattening filter. In the simulation which produced the phase space file, there was no magnetic field present. This has no impact on electron contamination properties as all contamination above the flattening filter is stopped by the filter itself, or the surrounding carosel base. The choice of generating the phase space without the presence of the MRI fringe field was made so that these data would reflect the most generic case, or a fully magnetically shielded region of the linac head. At this point in time it is unclear if such shielding will be required. As a quantitative measure of the impact of this approximation we also generated photon energy fluence maps of the phase space file which first included the fringe field and second for a $\pm$ 10% change in the electron beam FWHM cross sectional size striking the x-ray target. Both changes had insignificant differences in the energy fluence maps. In other words, the small fringe field had no significant impact on changing the resultant photon beam properties and hence phantom dose, and so the absence of the fringe magnetic field above the flattening filter is acceptable for this configuration simulated at 160 cm SID.

The simulation phantom consisted of a $30 \times 30 \times 30$ cm^3 water block positioned at isocenter. Thus the phantom surface was at 145 cm from the x-ray source. Scoring was performed in the entire phantom at a resolution of 1 mm^3, as well as at higher depth resolution in the first 1 mm depth. The surface resolution was in 10 μm thick layers in the first 0.1 mm and 0.1 mm thick layers from 0.1 mm to 1 mm depth. The 2D skin dose (at 70 μm effective depth) was calculated as the average of the dose in the 60-70 μm and 70-80 μm layers across the phantom surface. This is designed to match the definition of the effective skin dose depth as described in the ICRP Report 59.[34]

As a method to observe the path of electron contamination, the raw energy deposited per primary particle history in the phantom, helium, or air column, and linac head was extracted inside each simulation. The scoring grid resolution was 2 mm^3 and extended over a $30 \times 30 \times 150$ cm^3 volume (from isocenter to 150 cm above isocenter).

The ECD was implemented in the Monte Carlo environment with the same geometry and materials as the corresponding COMSOL model simulation. The only addition to the design was a 5 mm thick high density polyethlyene (HDPE) layer across the magnet and steel surfaces which faced the x-ray beam CAX direction. The HDPE cover was included in an effort to reduce backscattering of any deflected electrons which strike the magnet faces or steel. Without this there is an increased chance that these backscatter back into the beam path and become forced to travel towards the phantom surface.

The Monte Carlo particle step and cutoff parameters were set to 5 μm in the first 1 mm of the phantom (surface dose layers) and 0.2 mm in all other volumes. Selection of these step and cutoff parameters ensures that electrons are tracked correctly in air and under the influence of magnetic fields. Typically 6.5×10^{11} or greater primary particle histories were simulated to achieve less than $\pm$1% statistical error in the voxels located at D_{max} in the phantom at $1 \times 1 \times 1$ mm^3 resolution. The time taken for each different simulation was around 480 CPUh on 2.6 GHz AMD processors. This resulted in error estimates of $\pm$10% in the skin dose region voxels of 10 μm thick.

2.D. Helium gas region

The helium gas region was implemented in the Monte Carlo simulations by replacing the top 71.2 cm portion of the 81.2 cm air column between the ECD and phantom surface with helium gas. The final 10 cm air-gap between the helium region and phantom surface is deliberate and represents the extremity of the patient treatment volume where it would be impractical to place a helium gas region. It also corresponds to the lower edge of the cryostat wall and so is a practical location for termination of the helium region. To encase the helium gas a simple HDPE bag would be employed. This has been modeled as a 50 μm thick layer at the top and bottom of the helium gas region. This layer in fact acts as a source of secondary electron scatter and having its thickness as thin as practically possible is desirable.

3. RESULTS AND DISCUSSION

3.A. Reprocessed results from the 2001 Litzenberg experiments

Figure 2 shows some selected and reprocessed film data from the 2001 Litzenberg experiments. In the main figure body, central axis depth-dose profiles are presented for the films exposed to magnetic fields of B = 0 T, B = 0.5 T, and B = 3 T. Insert part (a) shows a zoomed plot of the first 3.5 cm

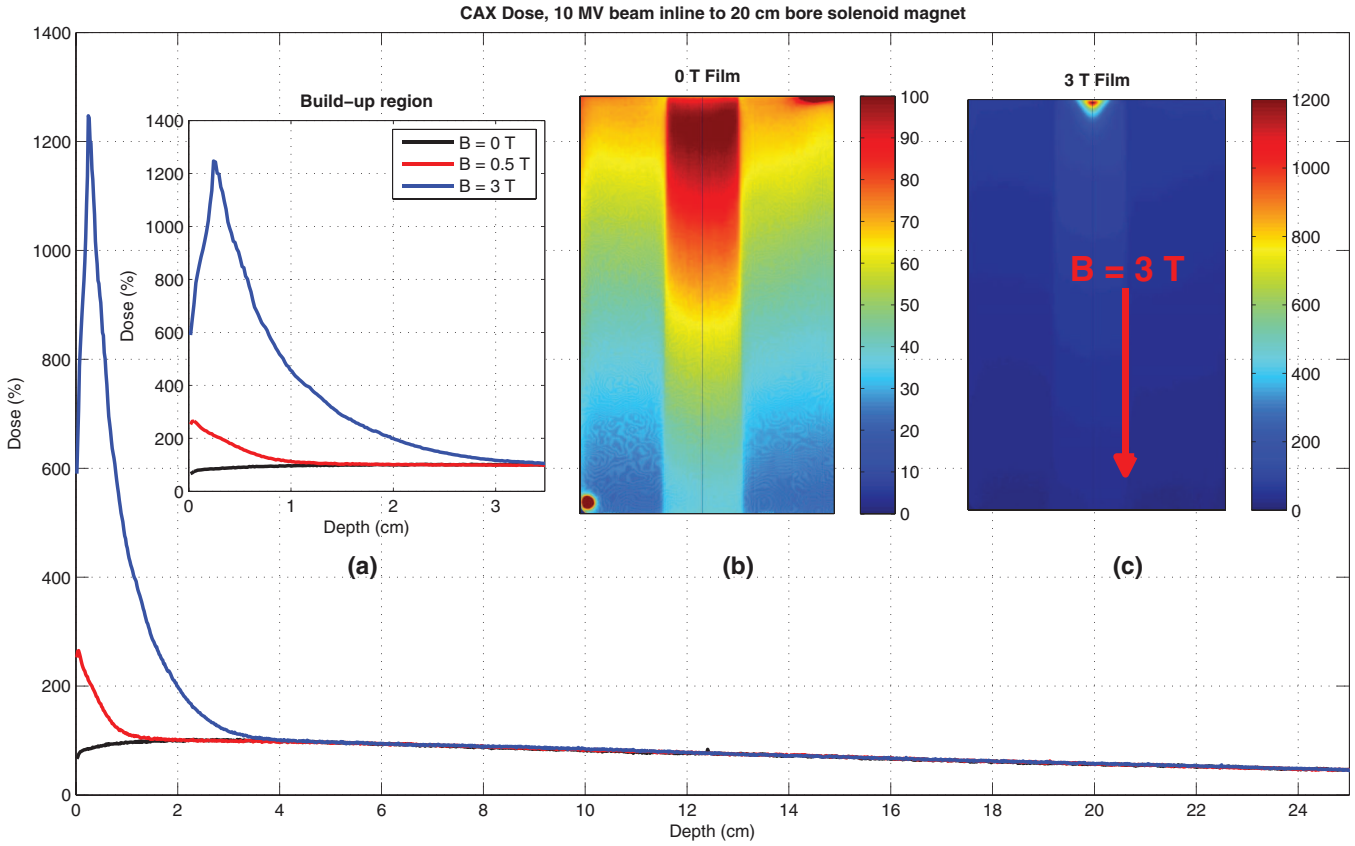

FIG. 2. Experimental evidence of an inline magnetic fringe field acting to increase surface dose. Data presented here are reprocessed films from the 2001 experimental work by Litzenberg *et al.* (Ref. 10). The main plot shows the central axis dose delivered by a 10 MV beam to a 20 cm diameter water phantom while exposed to 0 T, 0.5 T, and 3 T inline magnetic fields. Insert part (a) shows a zoom of the build-up region while (b) and (c) show the 0 T and 3 T films that were exposed. The high surface doses seen at 0.5 T and 3 T are due to electron contamination being focused by the fringe field.

depth while parts (b) and (c) show the 0 T and 3 T films which the plots were extracted from. There is a strong increase in the surface dose, particularly at 3 T. This is a direct product of the fringe field from the magnet acting to collect and focus air-generated contamination along the beam CAX, with the majority being near the magnet cryostat edge. The 3 T result also shows that the surface dose starts at $\sim$ 600% and increases to $\sim$ 1245% at $\sim$ 2.5 mm depth. This is opposed to the 0.5 T film showing a maximum dose of almost 270% at the surface. It is expected that this is either due to when exposed, the 3 T film was protruding slightly from the phantom in which it was positioned inside, or the electron contamination spectrum incident upon the surface to have a higher average energy than the 0.5 T case. In the former theory lateral scatter from the thin film would prevent the film from showing the maximum dose at the surface, while in the latter a larger build-up effect would be seen relative to the 0.5 T case. Either way it is clear evidence that a high surface dose due to contamination focusing is a real effect, and its magnitude can easily exceed the dose at D_{max}.

3.B. Benchmark magnetic modeling of the MRI design

Figure 3 shows a magnetic field magnitude ($|\vec{B}|$) plot through the magnet center for the 1 T MRI system as calculated by the manufacturer. Overlaid on this image is a contour line plot from our COMSOL simulations showing some of the magnetic field magnitude values. Two low field regions are also clearly identified and will be where the linac will reside in either the inline or perpendicular configurations. In this plot the color white is shown in regions above 2 T or below 0.06 T. An excellent match is seen between the contour and fill plots at the selected values of 0.06 T, 0.65, and 2 T. For a 30 cm DSV, we obtain a 6.8 ppm spread, or $\leq\pm$5 ppm. This matches the manufacturer's specifications of 1 T $\pm$5 ppm for a 30 cm DSV to within 4 decimal places. It is clear from Fig. 3 that an accurate model of our MRI system has been developed inside COMSOL which matches the manufacturer's specifications. This now gives us the ability to model the impact of a ferromagnetic ECD as described in Sec. 3.C.

3.C. Skin dose without an electron contamination deflector and helium gas region

To investigate the effect of SID variation on MRI-linac skin dose, Fig. 4 displays some key results from the Monte Carlo modeling. In each part the field size shown is 20 $\times$ 20 cm^2 at isocenter while the SID is varied from 100 cm to 130 cm and 160 cm.

In the top row is displayed the energy deposition along a central x-z slice (log-scale) throughout the linac head, air column, and phantom region. Superimposed on this is the

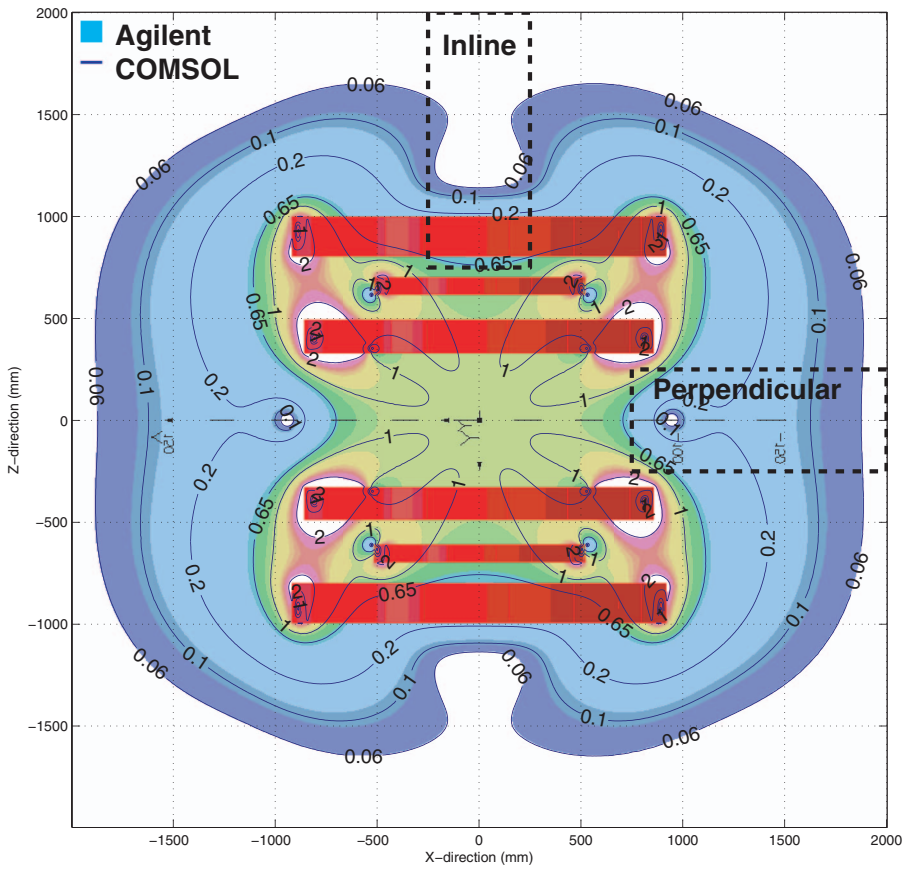

FIG. 3. Magnetic field magnitude map of the Agilent 1 T MRI design (fill plot) and COMSOL (contour plot) match in the central x-z plane. Current coils are shown in red and below 0.06 T or above 2 T is shown as white. The agreement seen between our COMSOL results and the Agilent data is ± 0.0001 T inside the DSV. Also shown is the low magnetic field regions for positioning of the linac in either the perpendicular or inline orientation.

magnetic field line directions [note Fig. 4(a) is without magnetic field]. In the middle row, the 2D skin dose at 70 μm depth is presented and in the bottom row the corresponding x/y profiles at 70 μm depth are compared with an average x/y profile at 15 mm depth.

In Fig. 4(a), the reference case of SID = 100 cm, and no magnetic field is shown. As expected the skin dose is around 23% for the 20 × 20 cm^2 field, and along the beam CAX there is a gradual drop-off in the energy deposition from the base of the flattening filter to the phantom level. This corresponds to electron contamination on average scattering away from the beam CAX. In Fig. 4(b), the MRI field is introduced and the impact on the contamination is immediately seen. Essentially contamination or in fact any scattered electron is trapped and encouraged to travel with the MRI field lines. Instead of spreading over a large area they are contained. Further to this, all forward scattered (toward isocenter) electrons produced by the flattening filter and ion chamber are collected and focused, rather than diverging away from CAX. Here with the 20 × 20 cm^2 field, we see the largest skin dose increase being around 29 times that of the dose at 1.5 cm depth, or D_{max} with a magnetic field at SID = 100 cm (29 × D_{max} for 10 × 10 cm^2, 24 × D_{max} for 5 × 5 cm^2). The fact that the skin dose is the same for 20 × 20 cm^2 and 10 × 10 cm^2 is evidence that this contamination arises mostly from the ion chamber and flattening filter. At 5 × 5 cm^2, there is a mild reduction as the jaws partially block some contamination.

As we go to SID = 130 cm [Fig. 4(c)], the same processes are acting; however, there is an overall stronger focusing effect, resulting in a smaller cross-section for where all the contamination will enter the phantom. On the other hand, the jaws are closed more to account for the extended SID, in effect blocking some contamination. This overall leads to even higher relative skin dose increases, in the order of 40 times that of the dose at D_{max} for B = 0 T and 20 × 20 cm^2 field (29 × D_{max} for 10 × 10 cm^2, 8 × D_{max} for 5 × 5 cm^2). This is higher than the SID = 100 cm case mostly due to the reduction in cross-sectional area of the hot-spot.

Finally, when we get to SID = 160 cm [Fig. 4(d)], there is a significant drop back to around 14 times the D_{max} dose (5.5 × D_{max} for 10 × 10 cm^2, 2.5 × D_{max} for 5 × 5 cm^2). This is attributed to both a natural purging of a portion of the contamination above the jaws, as well as the further closing of the jaws to account for SID = 160 cm. There is still a strong focusing of contamination below this level, as well as some propagation of electrons from the base of the flattening filter and ion chamber, particularly those generated near CAX.

In contrast to the high skin doses presented in this work, recent modeling work performed by the Alberta group on the skin/entry dose (average of the first 70 μm dose) increases for

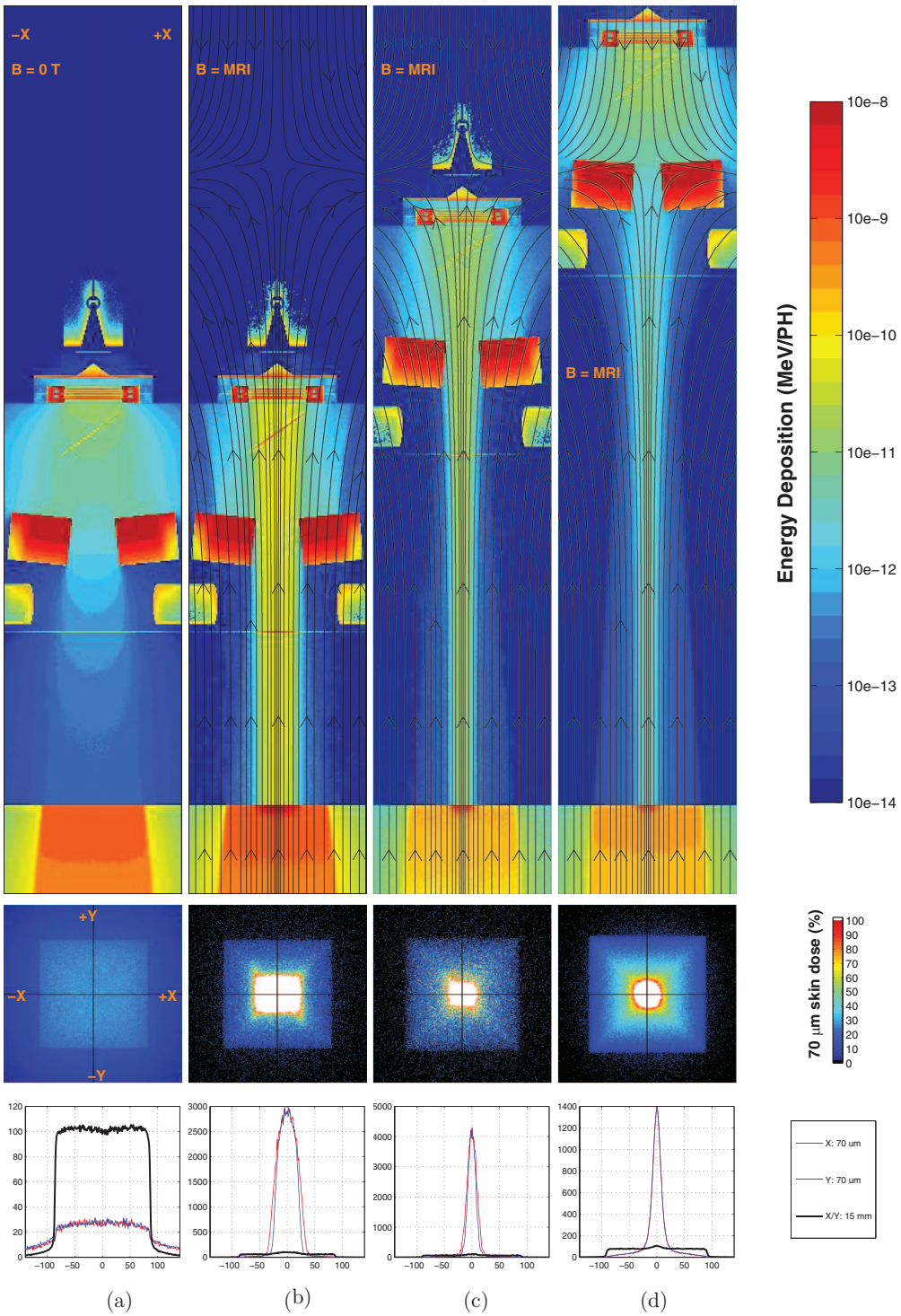

FIG. 4. Energy deposition (top row), 2D skin dose (middle row) and skin dose x/y profiles vs Dmax profiles (bottom row) for a 20 × 20 cm^2 field. In (a), we see no magnetic field and an SID of 100 cm. (b) shows the MRI field and an SID of 100 cm. (c) shows the MRI field and an SID of 130 cm. (d) shows the MRI field and an SID of 160 cm. In the top row, the energy deposition is on a log-scale to highlight the dose throughout the entire linac head, air column, and phantom region. In the middle row, the colormap is set to white at 100% dose or greater, and to black for < 2.5% dose. The skin dose hot spots are due to the MRI field acting to force a high majority of electron contamination particles to travel toward the CAX and the phantom surface, particularly those generated from the base of the flattening filter and ion chamber.

their prototype 126 cm SID, 0.56 T inline MRI-linac system was reported to be minor.[8] For that system the fringe field penetrating the linac head was modeled as insignificant and so they expect no contamination generated by the linac head to be collected and propagated towards the phantom. Only minor skin dose increases modeled were attributed to the final portion of the air column above the phantom having the same effect we see with contamination being transported directly to the phantom surface in the presence of the parallel magnetic field.

3.D. Electron contamination deflector modeling

3.D.1. Impact on the MRI imaging field

The inclusion of the various different ECD models had a direct impact on the 30 cm DSV uniformity ranging from 20 ppm up to 140 ppm (see Fig. 5). As expected the designs with the greatest mass of steel frame generated the largest nonuniformities. The total mass of the magnetic material had far less impact than the steel, primarily because the relative permeabililty of the magnet material is constant at 1.05 whereas the steel is ferromagnetic and has a strong BH-curve response in B-fields, especially below 0.5 T where the ECD lies. In Fig. 6(a), we see a plot of the magnetic field magnitude in the linac region without (left side) and with (right side) the heaviest ECD. For this ECD design, the magnet depth was 8 cm, the magnet thickness was 5 cm, and the steel thickness was 2.5 cm. This particular design has a 30 cm DSV distortion of 140 ppm which is well below the 300 ppm threshold for correction via passive shimming as indicated in previous work.[35] From Fig. 6(a), it is clear that this ECD gives rise to a very local perturbation of the fringe field, in particular in the x-direction.

Figure 6(b) shows the corresponding components of B_x, B_y, and B_z along the beam CAX with the presence of the heaviest ECD design. We note here that the B_x and B_y components at CAX without the ECD are very close to 0 T and so have been omitted for clarity. A maximum of 0.3 T transverse (B_x) field is generated between the magnet banks which causes the deflection process. It is expected that with utilization of passive shimming full imaging potential should be restored for the 1 T MRI system as the impact of the ECD at the DSV is not negligible, but within shimming tolerances.

3.D.2. Mechanical and design performance

The net force acting on the ECD was calculated to be between 151–1773 N and directed, due to obvious symmetry reasons, mostly toward the isocenter of the MRI-linac system. In the worst case senario where say the ECD is directly above isocenter we need to sum the magnetic force to the weight of the ECD to get the total force. These forces are relatively small and easily managed from a design perspective as it is expected to be mounted by a heavy duty aluminium frame that surrounds the ECD. This frame will be integrated into the generic supporting frame housing the linac MLCs. Hence from a design and construction point of view, the optimal ECD is viable.

There is one set of anomalies shown in Fig. 5 regarding the forces acting on the ECD. These are the three ECD models with the thinnest amount of steel and magnets (D = 4–8 cm, T = 1 cm, S = 0.5 cm). As expected the

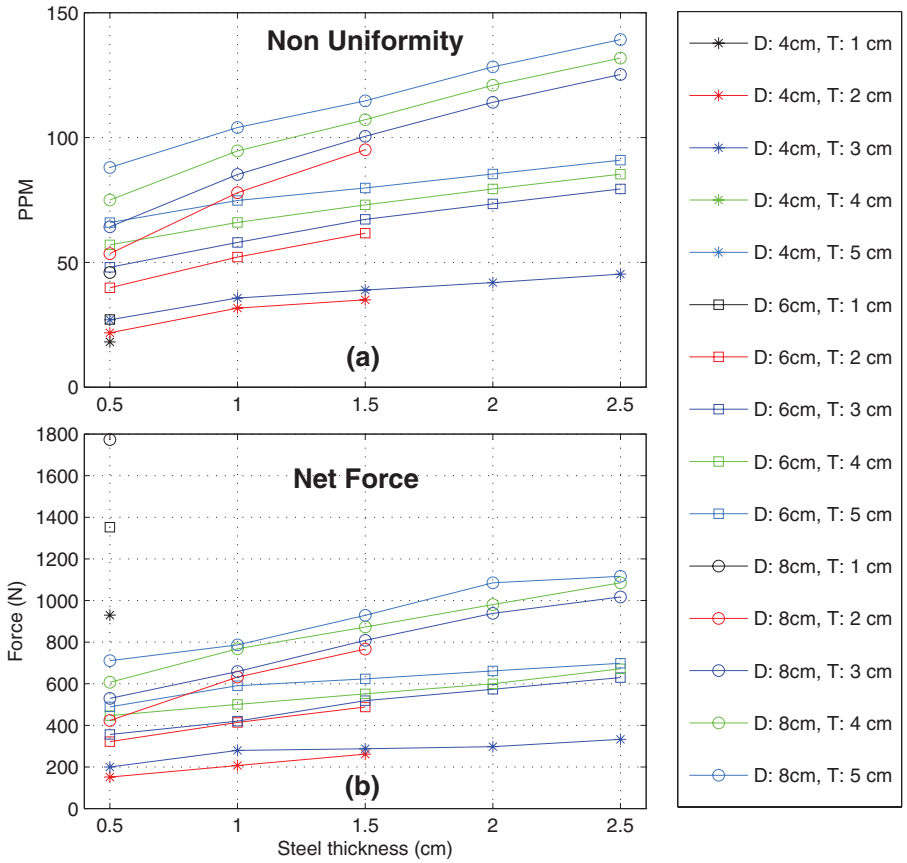

FIG. 5. Impact on the MRI uniformity and net forces acting on the ECD. In (a), we see the nonuniformity introduced by the ECD models. All models are <300 ppm and so will be correctable via active/passive shimming. In (b), we see the net force acting on the ECD. It is clear that increasing the overall mass of the ECD has a direct impact on the forces acting; however, these pose no engineering concerns. The anomaly seen with the forces acting on the 1 cm magnet thickness (T = 1 cm, S = 0.5 cm) models is attributed to the dominance of the MRI field over an inefficient magnetic circuit in the ECD.

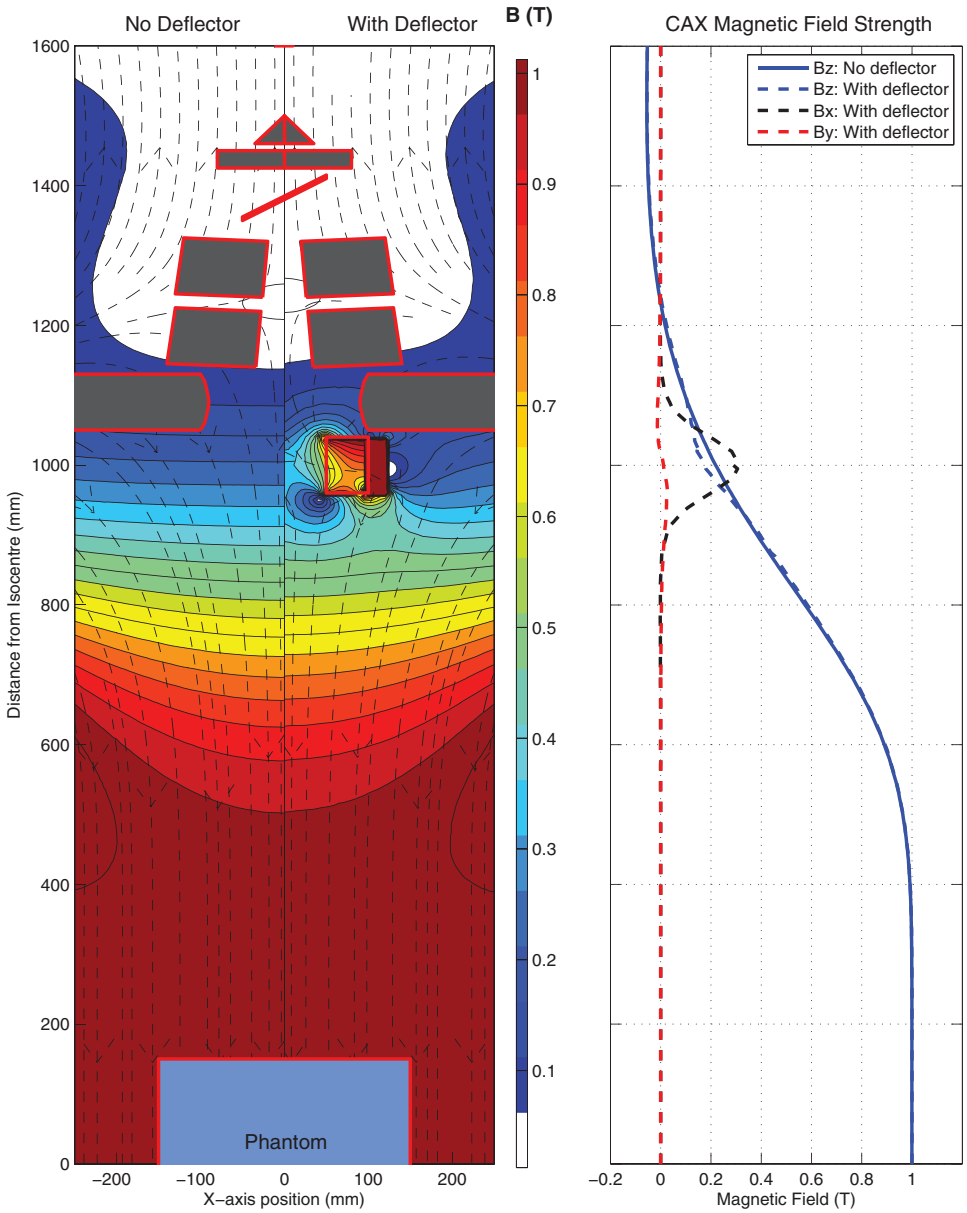

FIG. 6. Magnetic field properties encompassing the linac. (a) Left: No ECD, Right: With the heaviest ECD design present. Superimposed on these plots are MATLAB (Natick, Massachusetts) streamslice plots of the magnetic field (B_z) directions and linac components. In (b), plots of the magnetic field components along the CAX are shown. The ECD gives rise to a very localized B_x field which is used to purge the electron contamination.

nonuniformity introduced is some of the lowest; however, the forces are some of the highest. Inspection of the flux maps revealed that these 3 ECD models were not able to utilize the steel frame for flux focusing. The magnets were too small to encourage significant flux to travel across the gap or around the steel frame, especially considering that they are in the stronger background MRI fringe field in the z-direction. As a result, these ECD models generated only a small local perturbation to the MRI fringe field and so they were naturally strongly attracted toward the isocenter. In the next larger ECD designs (T = 2 cm, S = 1 cm), local flux changes were much stronger and the resultant forces dropped considerably. However, from that point the force increases approximately proportional to the mass of the steel in the model.

3.D.3. Performance on purging electron contamination

In terms of purging the electron contamination, the ideal ECD would generate a magnetic field that has only a B_x component, i.e., zero for the other components. This would mean that electrons traveling along the CAX in the $-z$ direction would undergo a force directed in the $-y$ direction, as detailed by the Lorentz force. However, in our case where the ECD fields are essentially superimposed onto the relatively

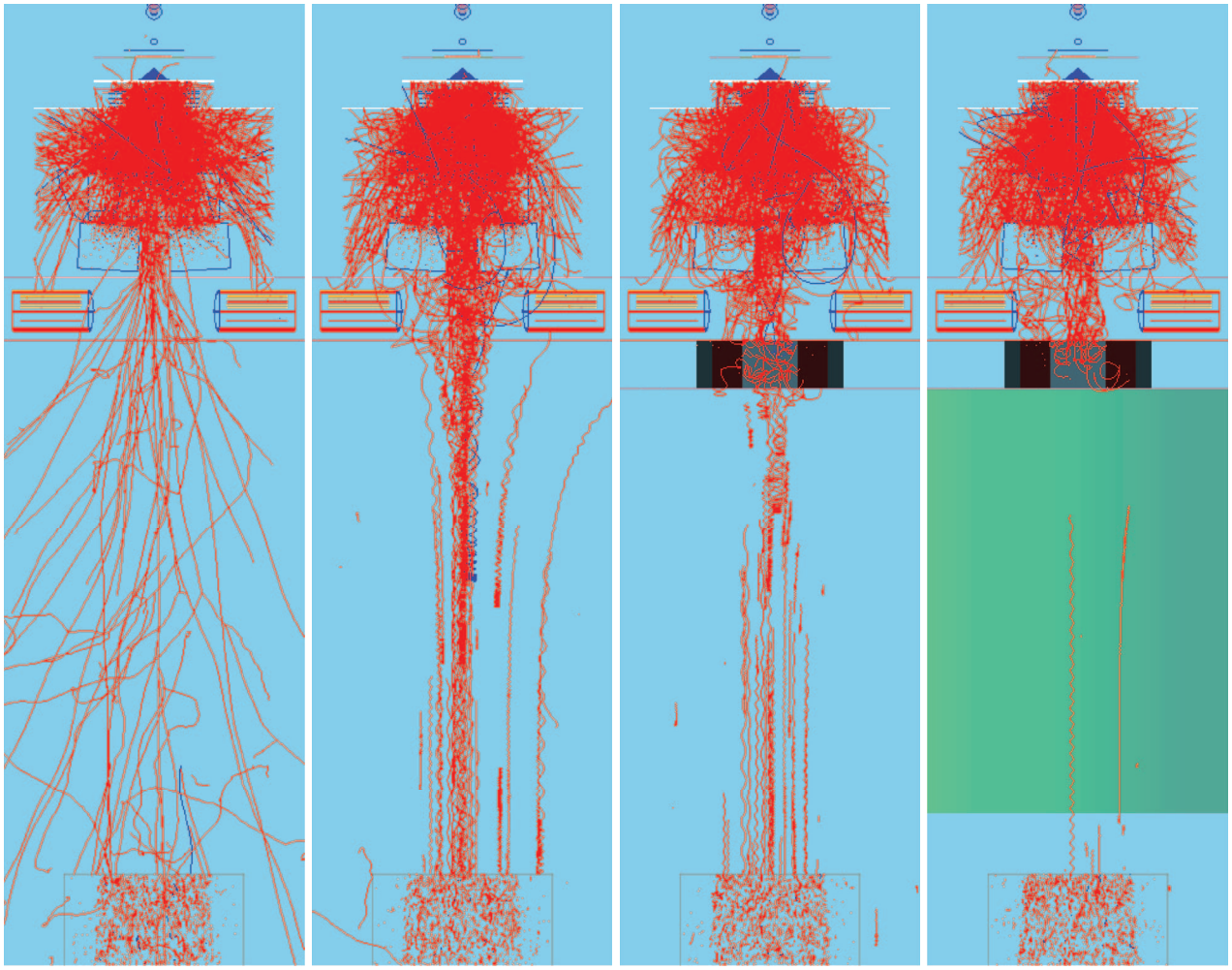

FIG. 7. Demonstration of the skin dose hot spot reduction by using the ECD and helium region: the electron contamination paths. In each plot, the SID = 160 cm, an x-ray field size of 20 × 20 cm^2 is shown, and 10 000 particles were fired from the phase space file at the base of flattening filter. (a) B = 0 T (no magnetic field). (b) B = MRI, same as (a) except the MRI field is included. (c) Inclusion of an optimal ECD. (d) Inclusion of an optimal ECD and helium gas region below the ECD of 71.2 cm. It is clear from parts (c) and (d) that in order to reduce the amount of electron contamination arriving at the phantom surface that a combination of both a ECD and helium gas region is required.

strong MRI fringe field in the z direction, the resultant magnetic force acting between the ECD magnet banks is comprised of approximately equal amounts of B_x and B_z, as seen in Fig. 6(b). Further to this the B_x and B_z forces are very different from each other above and below the central ECD level, and almost no electrons have only a z-component as they travel toward the ECD. Thus we can expect the electrons to be deflected in a much more complicated manner than just a simple −y direction force. Preliminary modeling confirmed this via visualization studies and so an immediate observation was that the majority of the higher energy electrons were purged into the -x side ECD magnet bank. It was evident then that these may be back-scattered, and return back to a similar origin, or conversely return to the beam path near CAX and continue to travel toward the phantom surface. In an effort to absorb these purged electrons rather than back-scatter them, the role of the HDPE magnet and steel covers was created. The ideal properties of this layer are (a) be nonmagnetic, (b) be as thin as possible to allow the magnet banks to be as close to a 20 × 20 cm^2 field edge as possible, and (c) be made from a material which discourages back-scattering. The choice of 5 mm of HDPE for this role is a first estimate. There is scope for altering this material and thickness however is not the focus of the current work.

In the simplest case the performance of the ECD is determined by its ability to purge linac head generated electron contamination as it passes through the ECD. Screen captures of the Geant4 simulations showing just the electron paths, along with examination of the energy deposition along the beam CAX is a useful method to observe this effect as shown in Fig. 7. Figure 7(a) shows the electron paths in the case of no magnetic field (B = 0 T), Fig. 7(b) shows the MRI field (B = MRI), Fig. 7(c) shows the MRI field with inclusion of an optimal ECD, and Fig. 7(d) shows the MRI field with the

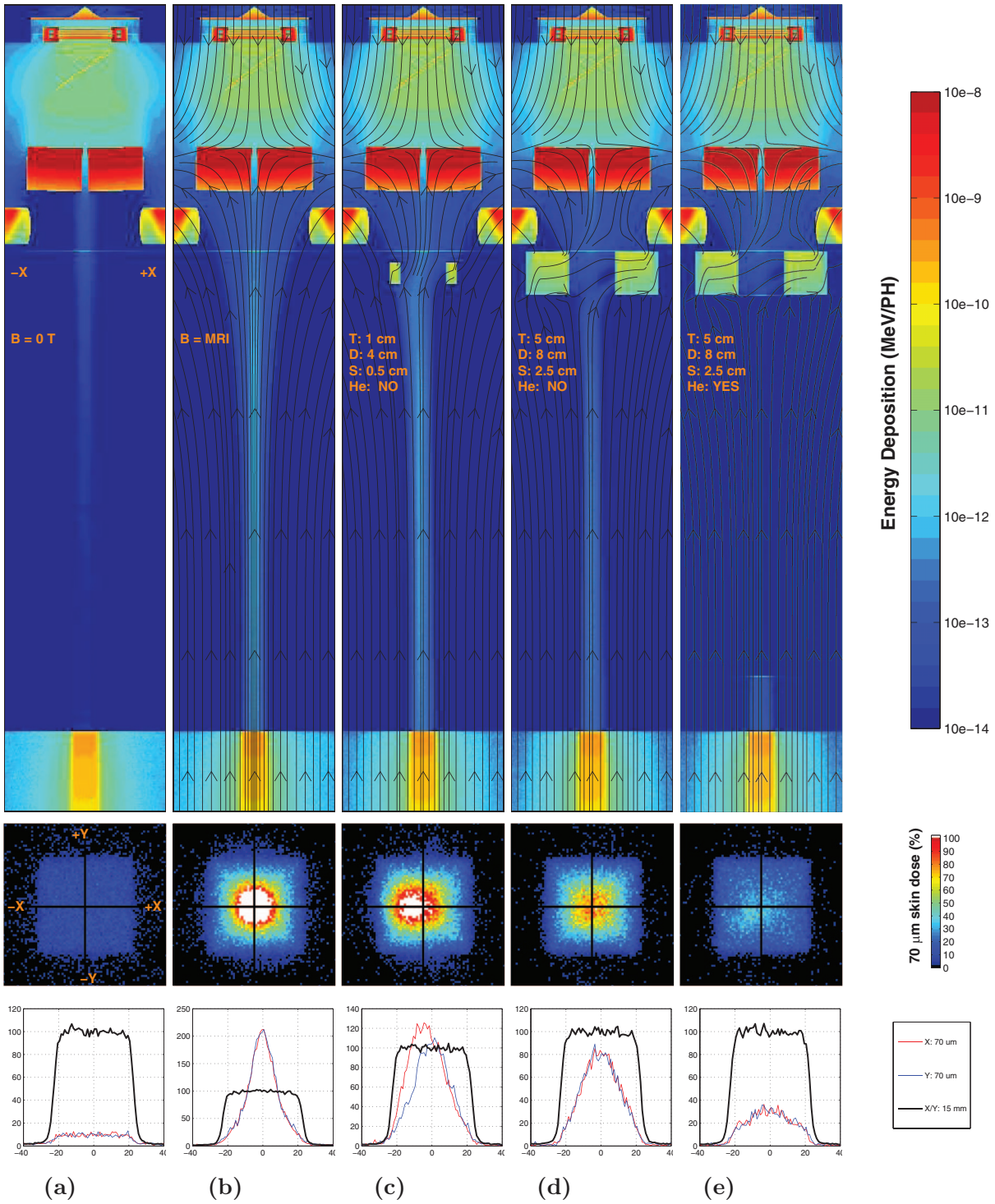

FIG. 8. Energy deposition (top row), 2D skin dose (middle row), and skin dose x/y profiles vs D_{max} profiles (bottom row) for a 5×5 cm^2 field. In (a), we see no magnetic field. (b) shows the MRI field. (c) shows the smallest and inefficient ECD design where not all head generated contamination is purged. (d) shows the most efficient ECD with air below while (e) shows the most efficient ECD with the addition of the helium region. In the top row, the energy deposition is on a log-scale to highlight the dose throughout the entire linac head, air column and phantom region. In the middle row, the colormap is set to white at 100% dose or greater, and to black for $< 2.5\%$ dose.

same ECD and the helium region. The field size in each of these images is 20×20 cm^2 and the SID is 160 cm.

It is immediately obvious in Fig. 7(b) how the MRI field acts to collect and focus the electron contamination. In Fig. 7(c) the process of electron contamination purging by the ECD is shown, however also shown is the reintroduction of air-generated contamination particles. Finally, in Fig. 7(d), the inclusion of the helium gas region minimizes air-generated contamination.

For a quantitative analysis, Figs. 8–10 show a summary of the key Monte Carlo simulation results for 5×5 cm^2, 10×10 cm^2, and 20×20 cm^2 beams with various ECDs.

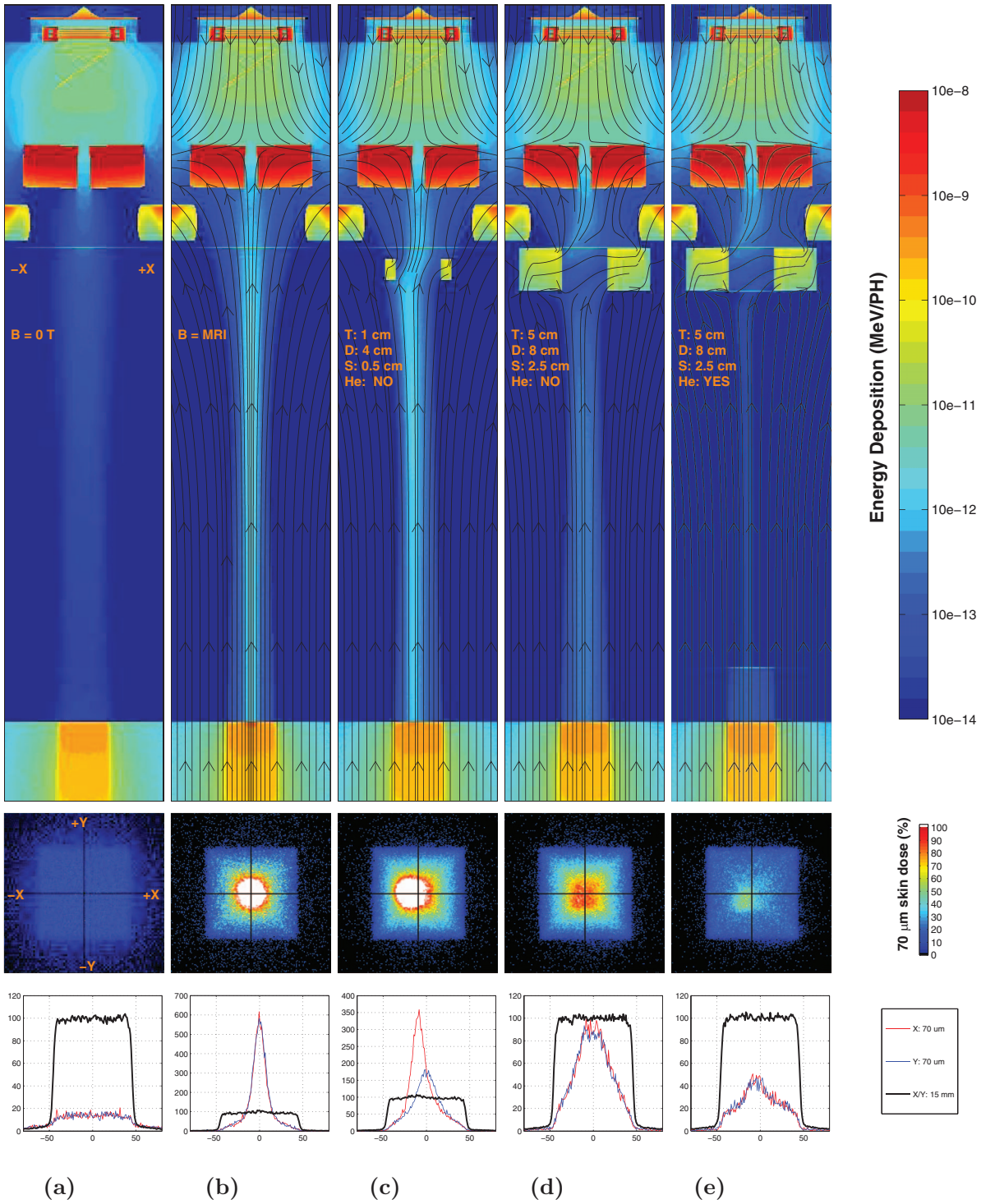

FIG. 9. Energy deposition (top row), 2D skin dose (middle row), and skin dose x/y profiles vs D_{max} profiles (bottom row) for a 10×10 cm^2 field. In (a), we see no magnetic field. (b) shows the MRI field. (c) shows the smallest and inefficient ECD design where not all head generated contamination is purged. (d) shows the most efficient ECD with air below while (e) shows the most efficient ECD with the addition of the helium region. In the top row, the energy deposition is on a log-scale to highlight the dose throughout the entire linac head, air column, and phantom region. In the middle row, the colormap is set to white at 100% dose or greater, and to black for $< 2.5\%$ dose.

In each of these figures, the top row shows the energy deposition per primary history (MeV/PH) along a central x-z plane with magnetic flux lines superimposed, the middle row shows the corresponding 2D skin dose map at 70 μm depth, and in the bottom row the corresponding x/y profiles at 70 μm depth are compared with an average x/y profile at 15 mm depth. Part (a) is the zero magnetic field case while part (b) is with the MRI field. Part (c) shows the lightest ECD design without the helium zone. The properties of the particular ECD modeled are noted in the top figure. Part (d) shows the most massive ECD without the helium region while part (e) includes the helium region for this ECD.

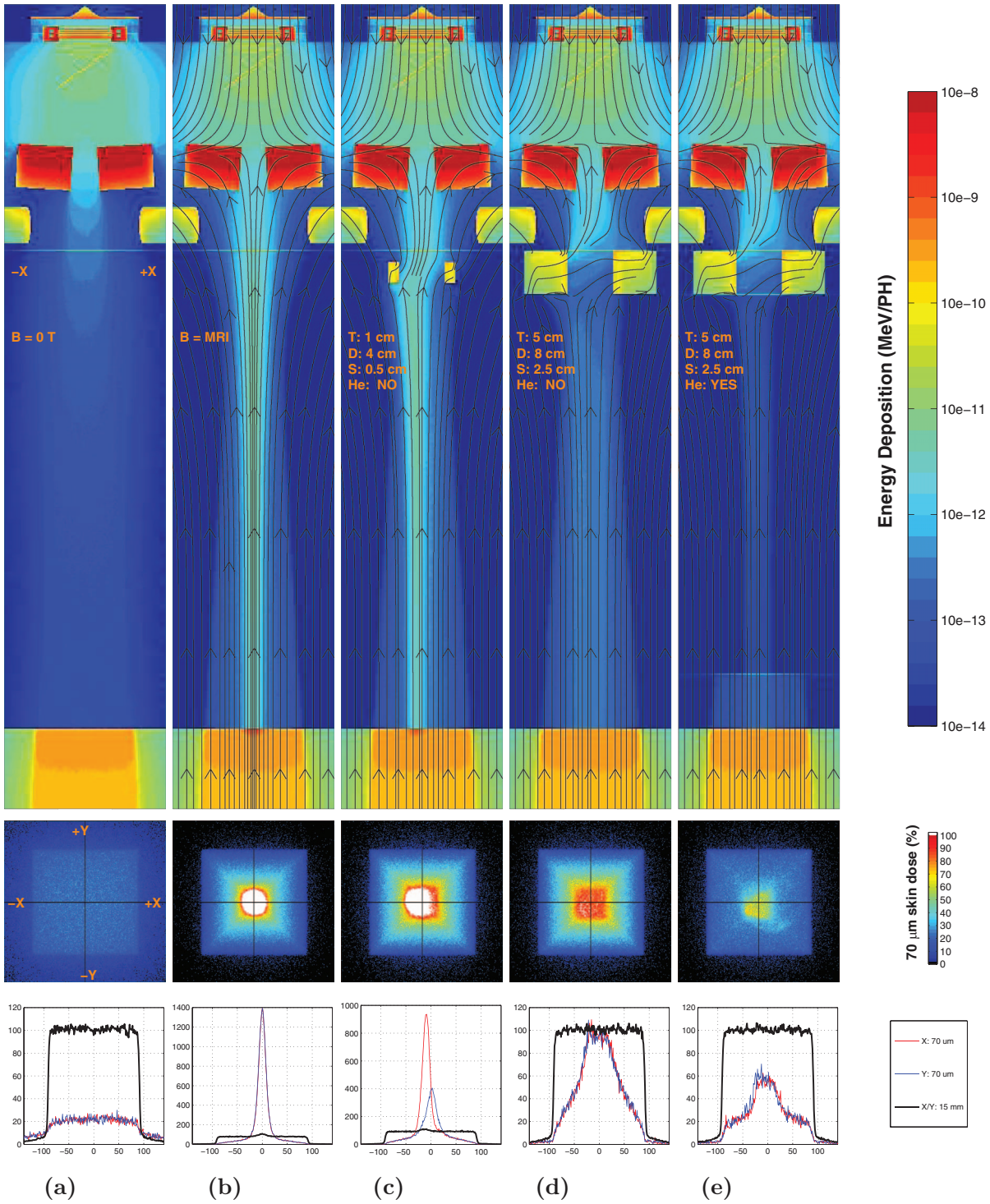

FIG. 10. Energy deposition (top row), 2D skin dose (middle row), and skin dose x/y profiles vs D_{max} profiles (bottom row) for a 20 × 20 cm^2 field. In (a), we see no magnetic field. (b) shows the MRI field. (c) shows the smallest and inefficient ECD design where not all head generated contamination is purged. (d) shows the most efficient ECD with air below while (e) shows the most efficient ECD with the addition of the helium region. In the top row, the energy deposition is on a log-scale to highlight the dose throughout the entire linac head, air column, and phantom region. In the middle row, the colormap is set to white at 100% dose or greater, and to black for < 2.5% dose.

The impact of an inefficient ECD is evident in parts (c) of each figure. There is simply not enough deflection occurring and the focused beam of electron contamination particles are allowed to pass through the ECD and still generate significant skin dose hot spots, however slightly shifted away from the beam CAX.

For the most efficient ECD designs [(part (d)], the assumption made is that all above ECD contamination is purged from the beam and that the resultant skin dose increases are primarily from a combination of (1) a flat fluence of direct x-ray beam induced dose, (2) a pyramid shaped fluence of air-generated electrons below the ECD, and (3) a complicated

fluence of electrons which scattered off the ECD magnet bank faces and returned to the beam traveling toward the isocenter. This is mostly confirmed in part (e) where the helium gas region is included. The 2D skin dose maps and profiles describe the final resultant hot spots as a combination of the base x-ray beam produced flat dose profile [compare with part (a)], a pyramid shaped and significant layer induced by the air-generated electrons, and a complex hot spot of smaller contribution which arises from any rescattered electrons from the ECD magnet bank faces. We should also note that there is some contribution as well from the upper and lower helium gas region windows which act as a source of electron scatter.

In the simplest terms, the only means for further reductions in skin dose would be to reduce the thickness of the helium gas region windows and to complete a study dedicated to optimizing the actual shape and surface properties of the ECD magnet banks and steel structure so that rescattering is minimized. Such a study is outside the scope of the current work.

In summary, there were 35 designs which gave almost identical and lowest skin dose hot spot increases for 5 $\times$ 5 cm^2. However, at 10 $\times$ 10 cm^2 only 23 models achieved complete purging, and for 20 $\times$ 20 cm^2 this was 14 designs. The reduction in efficiency for the larger field sizes is related to there being an increase in the amount of re-scattered electrons for the larger x-ray field sizes as compared to the 5 $\times$ 5 cm^2 case. This is because the x-ray beam passes closer by the ECD magnet bank faces for the larger field sizes, and hence there is a greater probability that scattered electrons will travel to the banks and back again.

4. CONCLUSION

In this work, we have modeled a prototype open bore 1 T inline MRI-linac system and have accurately matched the manufacturer's specifications on the characteristics of the MRI field. The accurate magnetic field map was used inside Geant4 Monte Carlo simulations to investigate our previous estimates on the expected high entry skin doses. For this system skin dose hotspots ranging from 230% of D_{max} for a 5 $\times$ 5 cm^2 to 1400% of D_{max} for a 20 $\times$ 20 cm^2 should be expected as the MRI field acts to collect and focus electron contamination as it travels toward the treatment volume. It should be noted that this result is unique to our 160 cm SID open bore design and so is not representative of lower field strength systems or smaller bore sizes.

In response to this issue, a permanent magnet style electron contamination deflector or ECD has been modeled for its performance in purging the contamination. Various ECD designs were highly efficient at purging the electron contamination from the x-ray beam; however, this does not eliminate the reproduction of electrons in the extended air-column of the prototype MRI-linac system, as well as some backscatter from the ECD itself. To address the former issue, a large and practical portion of the air column has been modeled as helium gas encased in a 50 μm thick HPDE bag. Monte Carlo simulations of this arrangement predict that purging of the contamination coupled with replacement of the air-column will act together to minimize the skin dose increases. The end result is a prediction that the 70 μm skin doses will moderately increase in a small hot-spot for the jaw defined field sizes of 5 $\times$ 5, 10 $\times$ 10, and 20 $\times$ 20 cm^2 to levels of 40%, 55%, and 65% of D_{max}. Surface doses of this magnitude represent small increases and as such should be practical in terms of expected patient skin dose response. The ECD is predicted to be a useful element of our 1 T prototype MRI-linac system.

[1] B. W. Raaymakers, J. J. W. Lagendijk, J. Overweg, J. G. M. Kok, A. J. E. Raaijmakers, E. M. Kerkhof, R. W. van der Put, I. Meijsing, S. P. M. Crijns, F. Benedosso, M. van Vulpen, C. H. W. de Graaff, J. Allen, and K. J. Brown, "Integrating a 1.5 T MRI scanner with a 6 MV accelerator: Proof of concept," Phys. Med. Biol. **54**, N229–N237 (2009).
[2] B. G. Fallone, B. Murray, S. Rathee, T. Stanescu, S. Steciw, S. Vidakovic, E. Blosser, and D. Tymofichuk, "First MR images obtained during megavoltage photon irradiation from a prototype integrated linac-MR system," Med. Phys. **36**, 2084–2088 (2009).
[3] J. F. Dempsey, D. Benoit, J. R. Fitzsimmons, A. Haghighat, J. G. Li, D. A. Low, S. Mutic, J. R. Palta, H. E. Romeijn, and G. E. Sjoden, "A device for realtime 3D image-guided IMRT," Int. J. Radiat. Oncol., Biol., Phys. **63**(2), S202 (2005).
[4] D. E. Constantin, R. Fahrig, and P. J. Keall, "A study of the effect of in-line and perpendicular magnetic fields on beam characteristics of electron guns in medical linear accelerators," Med. Phys. **38**(7), 4174–4185 (2011).
[5] B. M. Oborn, P. E. Metcalfe, M. J. Butson, and A. B. Rosenfeld, "High resolution entry and exit Monte Carlo dose calculations from a linear accelerator 6 MV beam under influence of transverse magnetic fields," Med. Phys. **36**(8), 3549–3559 (2009).
[6] B. M. Oborn, P. E. Metcalfe, M. J. Butson, and A. B. Rosenfeld, "Monte Carlo characterization of skin doses in 6 MV transverse field MRI-linac systems: Effect of field size, surface orientation, magnetic field strength, and exit bolus," Med. Phys. **37**(10), 5208–5217 (2010).
[7] B. M. Oborn, P. E. Metcalfe, M. J. Butson, A. B. Rosenfeld, and P. J. Keall, "Electron contamination modeling and skin dose in 6 MV longitudinal field MRIgRT: Impact of the MRI and MRI fringe field," Med. Phys. **39**(2), 874–889 (2012).
[8] A. Keyvanloo, B. Burke, B. Warkentin, T. Tadic, S. Rathee, C. Kirkby, D. M. Santos, and B. G. Fallone, "Skin dose in longitudinal and transverse linac-MRIs using Monte Carlo and realistic 3D MRI models," Med. Phys. **39**(10), 6509–6521 (2012).
[9] T. C. F. van Heijst, M. D. den Hartogh, J. J. W. Lagendijk, H. J. G. Desire van den Bongard, and B. van Asselen, "MR-guided breast radiotherapy: Feasibility and magnetic-field impact on skin dose," Phys. Med. Biol. **58**(17), 5917–5930 (2013).
[10] D. W. Litzenberg, B. A. Fraass, D. L. McShan, T. W. ODonnel, D. A. Roberts, F. D. Becchetti, A. F. Bielajew, and J. M. Moran, "An apparatus for applying strong longitudinal magnetic fields to clinical photon and electron beams," Phys. Med. Biol. **46**, N105–N115 (2001).
[11] Yu Chen, A. F. Bielajew, D. W. Litzenberg, J. M. Moran, and F. D. Becchetti, "Magnetic confinement of electron and photon radiotherapy dose: A Monte Carlo simulation with a nonuniform longitudinal magnetic field," Med. Phys. **32**(12), 3810–3818 (2005).
[12] B. Nilsson and A. Brahme, "Absorbed dose from secondary electrons in high energy photon beams," Phys. Med. Biol. **24**, 901–912 (1979).
[13] P. D. LaRiviere, "Surface dose from 6 MV photon interactions in air," Phys. Med. Biol. **28**, 285–287 (1983).
[14] E. D. Yorke, C. C. Ling, and S. Rustgi, "Air-generated electron contamination of 4 and 10 MV photon beams: A comparison of theory and experiment," Phys. Med. Biol. **30**, 1305–1314 (1985).
[15] R. Sjogren and M. Karlsson, "Electron contamination in high energy photon beams," Med. Phys. **23**(11), 1873–1881 (1996).
[16] M. J. Butson, P. K. N. Yu, and P. E. Metcalfe, "Incident contamination lepton doses measured using radiochromic film in radiotherapy," Radiat. Meas. **29**, 605–609 (1998).
[17] M. J. Butson, T. Cheung, P. Yu, and P. E. Metcalfe, "Evaluation of a radiotherapy electron contamination defecting system," Radiat. Meas. **32**, 101–104 (2000).
[18] A. L. Medina, A. Teijeiro, J. Garcia, J. Esperon, J. A. Terron, D. P. Ruiz, and M. C. Carrion, "Characterization of electron contamination in megavoltage photon beams," Med. Phys. **32**(5), 1281–1292 (2005).

[19]T. N. Padikal and J. A. Deye, "Electron contamination of a high-energy x-ray beam," Phys. Med. Biol. **23**, 1086–1092 (1978).
[20]P. J. Biggs and C. C. Ling, "Electrons as the cause of the observed shift in dmax with field size in high energy photon beams," Med. Phys. **6**, 291–295 (1979).
[21]C. C. Ling, M. C. Schell, and S. N. Rustgi, "Magnetic analysis of the radiation components of a 10MV photon beam," Med. Phys. **9**, 20–26 (1982).
[22]P. J. Biggs and M. D. Russell, "An investigation in the presents of secondary electrons in megavoltage photon beams," Phys. Med. Biol. **28**, 1033–1043 (1983).
[23]G. Krithivas and S. N. Rao, "A study of the characteristics of radiation contaminants within a clinically useful photon beam," Med. Phys. **12**, 764–768 (1985).
[24]B. R. Thomadsen, S. S. Kubsad, B. R. Paliwal, S. Shahabi, and T. R. Mackie, "On the cause of the variation in tissue-maximum ratio values with source-to-detector distance," Med. Phys. **20**(3), 723–727 (1993).
[25]D. M. D. Frye, B. R. Paliwal, B. R. Thomadsen, and P. Jursinic, "Intercomparison of normalized head-scatter factor measurement techniques," Med. Phys. **22**(2), 249–253 (1995).
[26]P. A. Jursinic and T. R. Mackie, "Characteristics of secondary electrons produced by 6, 10 and 24 MV x-ray beams," Phys. Med. Biol. **41**, 1499–1509 (1996).
[27]M. J. Butson, T. P. Y. Wong, A. Law, M. Law, J. N. Mathur, and P. E. Metcalfe, "Magnetic repulsion of linear accelerator contaminants," Med. Phys. **23**(6), 953–955 (1996).
[28]R. Sjogren and M. Karlsson, "Influence of electron contamination on *in vivo* surface dosimetry for high-energy photon beams," Med. Phys. **25**(6), 916–921 (1998).
[29]COMSOL Multiphysics, Stockholm, Sweden.
[30]S. Kolling, B. Oborn, and P. Keall, "Impact of the MLC on the MRI field distortion of a prototype MRI-linac," Med. Phys. **40**(12), 121705 (10pp.) (2013).
[31]S. Agostinelli *et al.*, "Geant4-a simulation toolkit," Nucl. Instrum. Methods Phys. Res., Sect. A **506**, 250–303 (2003).
[32]A. J. E. Raaijmakers, B. W. Raaymakers, and J. J. W. Lagendijk, "Experimental verification of magnetic field dose effects for the MRI-accelerator," Phys. Med. Biol. **52**, 4283–4291 (2007).
[33]Varian Medical Systems, Palo Alto, CA.
[34]International Commission on Radiological Protection, "ICRP Publication 60, 1990 Recomendations of the Internation Commission on Radiological Protection," Annals of the ICRP **21**(1–3), 41 (1991).
[35]L. Liu, H. Sanchez-Lopez, F. Liu, and S. Crozier, "Flanged-edge transverse gradient coil design for a hybrid LINAC-MRI system," J. Magn. Reson. **226**, 70–78 (2013).